
Numerical Investigation of Axial Magnetic Field Effects on Melt Flow and Macrosegregation in TC17 Alloy Vacuum Arc Remelting

Chenbo Xu ^{a,b}, Jie Guo ^a, Jincheng Wang ^a, Junjie Li ^{a*},
Liqing Huang ^c, Kai Fan ^c, Haijie Zhang ^b and Menghuai Wu ^{b*}

DOI: <https://doi.org/10.9734/bpi/mono/978-93-49473-95-9/CH4>

Peer-Review History:

This chapter was reviewed by following the Advanced Open Peer Review policy. This chapter was thoroughly checked to prevent plagiarism. As per editorial policy, a minimum of two peer-reviewers reviewed the manuscript. After review and revision of the manuscript, the Book Editor approved the manuscript for final publication. Peer review comments, comments of the editor(s), etc. are available here: <https://peerreviewarchive.com/review-history/3590.4>

ABSTRACT

The TC17 alloy ingot is produced through vacuum arc remelting (VAR). However, the self-induced electromagnetic force enhances forced convection, which can lead to potential macrosegregation, particularly as the ingot diameter increases. To address this issue, an engineering solution involves applying an axial magnetic field (AMF) to modify the flow in the molten pool. In this study, the solidification process of the VAR ingots was simulated using a built-in solidification model in ANSYS Fluent. The solver is based on the finite volume method. A 2D-axisymmetric simulation considering the swirl flow was performed, incorporating the multi-physics coupling of heat transfer, solute transfer, melt flow, and electromagnetic effects. The reasonable agreement between the simulation and experiment regarding the molten pool contour and segregation profile demonstrates the robustness and applicability of the model. On this base, a numerical parameter study was performed to study the effect of the AMF, with particular emphasis on the alternative AMF direction change and the resulting melt flow. The results show that the applied AMF generates an electromagnetic force in the tangential direction, creating a rotational swirl flow and a centrifugal force directed radially outward. Consequently, a secondary flow along the side walls towards the bottom centre within the molten pool is induced. This modified flow pattern in the molten pool helps reduce macrosegregation in VAR ingots, hence

^a State Key Laboratory of Solidification Processing, Northwestern Polytechnical University, Xi'an 710072, China.

^b Department of Metallurgy, Montanuniversität Leoben, Franz-Josef Street 18, 8700 Leoben, Austria.

^c Hunan Goldsky Titanium Industry Technology Co., Ltd., Changde 415001, China.

*Corresponding author: E-mail: menghuai.wu@unileoben.ac.at, lijunjie@nwpu.edu.cn;

improving the service life and mechanical properties of aviation titanium alloys. Qualitative simulation-experiment agreement regarding the shape of the molten pool profile and segregation distribution is achieved. However, future model improvement, e.g. considering the solidification crystal morphology, multiphase flow, and potential formation of freckles, is necessary.

Keywords: Vacuum arc remelting (VAR); numerical simulation; melt flow; macrosegregation; axial magnetic field (AMF); TC17 alloy.

4.1 INTRODUCTION

The TC17 alloy (Ti-5Al-2Sn-2Zr-4Cr-4Mo) is widely employed in the aviation industry due to its high specific strength, exceptional fracture toughness, and corrosion resistance [1,2]. Vacuum arc remelting (VAR) has become the predominant method for producing TC17 alloy ingots. As shown in Fig. 4.1(a), raw materials are formed into a consumable electrode, serving as the cathode, while a water-cooled copper crucible functions as the anode. The consumable cathode is rapidly melted by the high temperature of a direct current (DC) arc in a vacuum atmosphere, to form the droplets. They pass through the high-temperature arc zone and solidify in a water-cooled copper crucible. In practical production, however, several metallurgical defects, such as macrosegregation, shrinkage, nonmetallic inclusions, and uneven structure, remain unavoidable in the as-cast ingot. Among these, macrosegregation is one of the most prevalent defects, primarily caused by the melt flow in the molten pool. Kondrashov et al. [3] experimentally determined the solute concentration in the VAR ingot of Ti-6Al-4V alloy, noting that the susceptibility to segregation and its extent is largely dictated by the solute equilibrium partition coefficient.

Traditional experimental research is costly and does not permit direct observation of melt flow dynamics within VAR ingots, making it impossible to study the mechanisms of macrosegregation. Davidson et al. [4,5] simulated the liquid phase flow in the molten pool during the VAR process, analyzing the flow patterns induced by buoyancy, self-induced electromagnetic forces, and stirring electromagnetic forces. Kondrashov et al. [6] developed a simplified solidification model that disregarded the influence of the electromagnetic field on fluid motion. By considering gap heat transfer, they simulated the temperature distribution and molten pool morphology during the solidification of VT3-1 alloy, achieving results consistent with experimental data. Karimi-Sibaki et al. [7,8] examined the impact of axial magnetic fields in the VAR process of Ti-6Al-4V alloy, demonstrating that adjustments to the strength and direction of the axial magnetic field significantly influenced the shape of the molten pool and the melt flow. More recently, some researchers have also explored the effects of process parameters such as melting current intensity, thermal boundary conditions and external magnetic field intensity on solidification structure and composition distribution [9–11]. However, these studies have yet to establish a clear relationship between macrosegregation in VAR ingots and flow patterns. Unlike previous studies, this work explicitly establishes a relationship between macrosegregation patterns and flow dynamics during VAR with AMF.

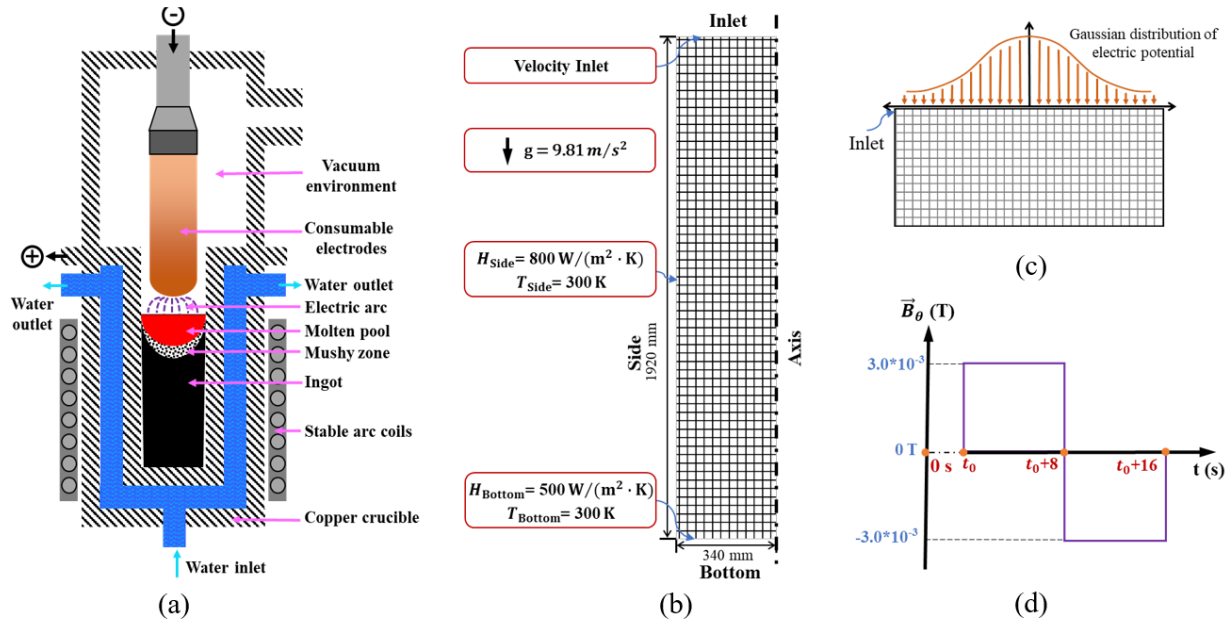


Fig. 4.1. Simulation configuration. (a) schematic of VAR, (b) casting dimension and boundary conditions, (c) the Gaussian distribution of electric potential applied on the domain inlet, (d) the external magnetic flux density \vec{B}_θ induced by external AMF.

In the present study, the solidification process of VAR ingot is numerically simulated using Ansys Fluent 16.0. The TC17 alloy is simplified as a Ti-Zr binary alloy. A 2D-axisymmetric simulation considering the swirl flow is performed, accounting for the effects of combined thermal and solute-driven buoyancy force, self-induced electromagnetic force, and stirring electromagnetic force generated by external AMF in the momentum conservation equation. The macrosegregation is modelled by solving the species transport equation. The primary objective is to achieve a fundamental understanding of the effects of various forces (i.e., \vec{F}_B , \vec{F}_L , and \vec{F}_T) on melt flow, and to build a qualitative correlation between the liquid flow and the development of macrosegregation.

4.2 MODELING

4.2.1 Model Description and Key Assumptions

The solidification processes are modeled using the enthalpy-porosity approach proposed by Voller et al. [12,13]. The governing equations, including the continuity, energy, and solute conservation equations, closely align with those presented in the existing literature [4,14]. The multicomponent TC17 alloy is simplified as a binary Ti-Zr alloy with a nominal Zr concentration of 1.97 %. The possible formation of equiaxed crystals is ignored, and the solidification crystal morphology is assumed as columnar with a porous medium in the mushy zone. The flow permeability of the mushy zone is described by Darcy's law and is solved using the Blake-Kozeny equation [15], which relates to the secondary dendrite arm spacing and the solid phase volume fraction.

In order to couple multiple forces in the current model, the Boussinesq approximation is employed to account for the combined thermal and solute buoyancy, incorporating both the solutal (β_c) and thermal (β_T) expansion coefficients. During the ingot remelting process, a closed loop of electric current is formed through the power supply, electrode, arc, ingot, and crucible, generating a self-induced magnetic field. The interaction between the remelting current and this self-induced magnetic field produces the self-induced electromagnetic force. The external AMF is introduced through an alternating current (AC) passing through external coils, which interacts with the remelting current to generate the stirring electromagnetic force.

4.2.2 Boundary Conditions

As shown in Fig. 4.1(b), the side and bottom of the ingot serve as convection heat transfer boundaries, while the top boundary is established as a temperature boundary, with the primary heat input originating from the DC arc's action throughout the casting operation. This setting of boundary conditions follows what is outlined in the literature [6]. The electric potential for both the side and the bottom walls of the ingot is assigned to be zero value, while a Gaussian distribution of electric potential is applied to the top boundary, as shown in Fig. 4.1(c). For the flow calculation, the side and bottom boundaries of the ingot are treated as no-slip

boundaries, while the top boundary is designated as a velocity inlet. Utilizing the dynamic mesh functionality in the ANSYS Fluent, the remelting rate of the ingot is coupled with the mesh growth rate, facilitating the dynamic increase in ingot height during the casting process. The solute composition of the melt at the top boundary is set as the nominal composition, and the solute gradient at the other boundary is set to zero value.

4.2.3 Simulation Parameters

These parameters/properties employed in the simulation are detailed in Table 4.1.

Table 4.1. TC17 Physical Properties and Simulation Parameters

Parameters	Symbols	Values	Units
Initial concentration of Zr	c_{Zr}	1.97	wt. %
Partition coefficient of Zr	k_{Zr}	0.85	—
Liquidus slope	m_{Zr}	-8686.9	$K \cdot (\text{wt}\%)^{-1}$
Density	ρ	4320.0	$\text{kg} \cdot \text{m}^{-3}$
Liquid diffusion coefficient	D_ℓ	5.0×10^{-9}	$\text{m}^2 \cdot \text{s}^{-1}$
Solute expansion coefficient	β_c	-0.4	wt. \%^{-1}
Temperature expansion coefficient	β_T	6.5×10^{-4}	K^{-1}
Liquidus temperature	T_ℓ	1930.2	K
Solidus temperature	T_s	1900.2	K
Mushy zone parameters	A_{Mush}	7.67×10^6	$\text{kg} \cdot \text{s}^{-1} \cdot \text{m}^{-3}$
Viscosity	μ_ℓ	3.1×10^{-3}	$\text{kg} \cdot \text{m}^{-1} \cdot \text{s}^{-1}$
Specific heat	c_p	975.0	$\text{J} \cdot \text{kg}^{-1} \cdot \text{K}^{-1}$
Thermal conductivity	K_T	33.0	$\text{W} \cdot \text{m}^{-1} \cdot \text{K}^{-1}$
Electrical conductivity	σ	1.1×10^6	$\text{S} \cdot \text{m}^{-1}$
Magnetic permeability	μ_0	1.26×10^{-6}	$\text{H} \cdot \text{m}^{-1}$
Gibbs-Thomson coefficient	Γ	5.37×10^{-7}	$\text{K} \cdot \text{m}$

4.3 SIMULATION RESULTS AND ANALYSIS

A quasi-steady state is reached approximately 9600 s into the VAR process. As shown in Fig. 4.2(a), the isotherms are characterized by a distinct “V”-shaped morphology, which is also reflected in the shape of the molten pool in Fig. 4.2(g). The buoyancy force \vec{F}_B is determined by both the temperature and solute distribution within the molten pool. Because the solute enrichment in the molten pool is ignorable, \vec{F}_B is dominated by the thermal field, Fig. 4.2(b). The vectors in Fig. 4.2(c) depict the electric current path, and the electric current \vec{j} converges at the center of the ingot top surface. According to the Ampere's Law, such distribution of \vec{j} results in the self-induced magnetic flux density \vec{B} field presented in Fig. 4.2(d). The interaction between \vec{j} and \vec{B} generates the self-induced electromagnetic force \vec{F}_L directed toward the axis of the ingot. As depicted in Fig. 4.2(e), \vec{F}_L is predominantly located in the upper portion of the molten pool,

while the lower region remains unaffected. Additionally, the application of an external AMF interacts with the current density \vec{j} to produce the stirring force \vec{F}_T , Fig. 4.2(f). Different from \vec{F}_B , \vec{F}_T acts in the tangential direction. Under the combined influence of \vec{F}_B , \vec{F}_L and \vec{F}_T , two vortices in the vertical section of the ingot are generated within the molten pool, rotating in opposite directions, Fig. 4.2(g). The counterclockwise vortex is significantly more pronounced, and the maximal velocity is up to 0.09 m/s. The flow in the tangential direction is not shown. The mechanism of how the acting forces influence the flow pattern will be discussed later. This analysis highlights the intricate interplay of forces during the solidification of TC17 alloy VAR ingots, underscoring the critical roles of electromagnetic and buoyancy-driven flow phenomena in influencing the resultant flow and thermal field.

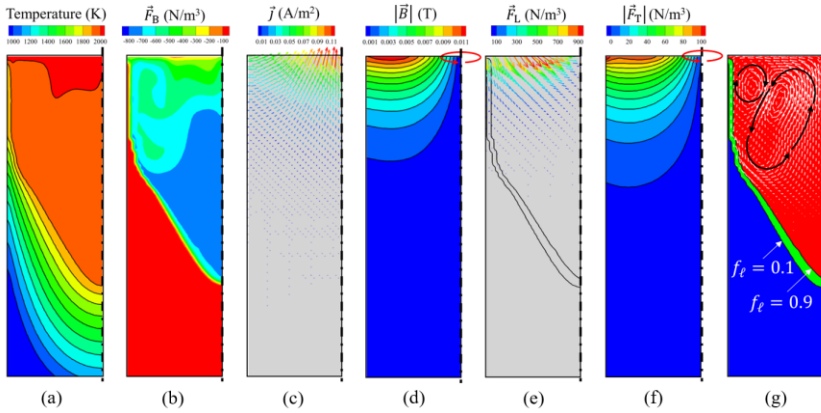


Fig. 4.2. Simulation results (only left half of the ingot) at remelting time 9600 s when quasi-steady state is reached. Distributions of (a) temperature, (b) \vec{F}_B , (c) electric current density \vec{j} , (d) self-induced magnetic flux density \vec{B} , (e) \vec{F}_L , (f) \vec{F}_T , (g) velocity. The molten pool shape is marked in (g) with a liquid volume fraction of $f_\ell = 0.1$ and 0.9 .

The simulation-experiment comparison is shown in Fig. 4.3. The calculated molten pool traces at different time intervals were overlaid on the as-cast structure in Fig. 4.3(a). The crystal growth direction is almost perpendicular to the molten pool traces, which indicates the consistency between the experiment and simulation. In terms of solute distribution (Zr) within the ingot, samples were collected from five heights at both the periphery and center of the upper half of the VAR ingot, as shown by the blue and red triangles in Fig. 4.3(a). The solute concentration for the collected samples was analyzed using inductively coupled plasma atomic emission spectrometry (ICP). The calculated and measured solute concentration along the ingot height at both the periphery and center is shown in Fig. 4.3(b). Both the simulation and experimental results reveal similar solute concentration distribution trends. Specifically, the Zr concentration at the periphery is slightly

lower compared to the center. Additionally, as the height of the ingot decreases, a noticeable reduction in Zr concentration is observed in the central area, while the Zr concentration at the periphery remains relatively constant along the height.

4.4 DISCUSSION

During the VAR process, the fluid flow alters the solute and temperature fields, thereby influencing the molten pool morphology and ultimately determining the macrosegregation pattern. The melt flow is influenced by three different forces, i.e., \vec{F}_B , \vec{F}_L and \vec{F}_T . In this section, three cases with varying force combinations were numerically investigated, and the simulation results are displayed in Fig. 4.4. In Case I, only \vec{F}_B is considered; in Case II, both \vec{F}_B and \vec{F}_L are considered, and all these three forces are considered in Case III.

4.4.1 Case I: Considering only \vec{F}_B

The simulation results of Case I is shown in Fig. 4(a). The melt flow pattern remains consistent throughout the VAR process. During the solidification process, the solute element Zr is rejected into the interdendritic liquid. Both solute enrichment and lateral cooling increase the density of the liquid near the solidification front. Thereby, a counterclockwise vortex is developed on the left side of the molten pool. The liquid near the top surface flows from the center towards the side boundary of the crucible. It then turns and flows along the solidification front to the bottom of the molten pool, rising back up along the central axis to the top surface. The liquid velocity is about 0.01 m/s at the surface of the molten pool, while the flow in the bottom and central areas is much weaker. Different from the results that were shown in Fig. 4.2(a), this reduced liquid flow results in temperature stratification. The current results are consistent with the findings of Davidson et al. [5].

4.4.2 Case II: Considering \vec{F}_B and \vec{F}_L

In the axisymmetric system, the magnetic fields produced by the radial current components of electric current cancel each other. Therefore, only the magnetic field \vec{B} , which is produced by the axial component of electric current, interacts with the electric current to generate the Lorentz force \vec{F}_L . As illustrated in Fig. 4.4(b), \vec{F}_L points towards the lower center of the molten pool. Both \vec{F}_B and \vec{F}_L operate together, but \vec{F}_L predominantly concentrated near the upper surface of the ingot. When the VAR process reaches the quasi-steady state, \vec{F}_L predominantly dictates the flow field in the upper molten pool, creating a strong “center downward, periphery upward” flow pattern, with a maximum velocity of approximately 0.12 m/s. In the lower molten pool region, where the electromagnetic force \vec{F}_L is significantly reduced, the role of the buoyancy force \vec{F}_B becomes more pronounced. This leads to a predominant flow pattern characterized by a milder “periphery downward, center upward” movement.

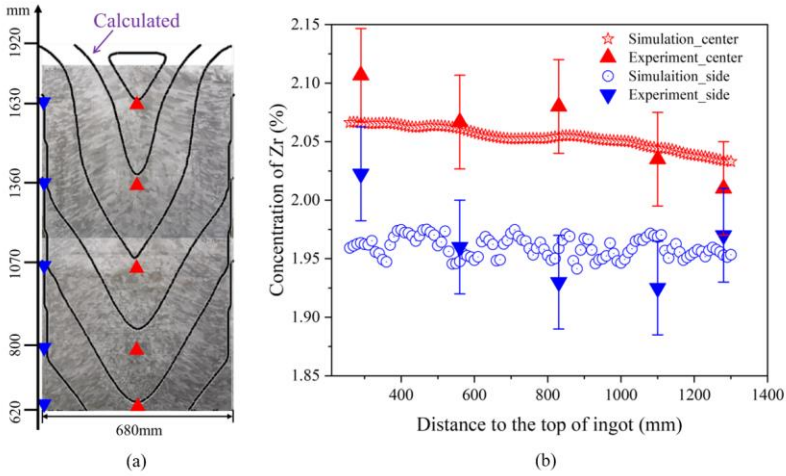


Fig. 4.3. Model validation. (a) The as-cast structure overlaid by the calculated molten pool profiles, the red and blue triangles denote the sampling sites for solute concentration measurements, (b) comparison of Zr distribution along the sample height.

4.4.3 Case III: Considering all three Forces \vec{F}_B , \vec{F}_L and \vec{F}_T

In addition to the \vec{F}_B and \vec{F}_L , an AMF-induced electric magnetic force \vec{F}_T , acting in the tangential direction, is applied. The external AMF is generated by a 12 A alternating arc-stabilizing current through the external coils. The alternating period of the arc-stabilizing current is 16 s, resulting in a reversal of the external magnetic flux density \vec{B}_θ every 8 s, Fig. 4.1(d).

Fig. 4.4(c) illustrates the flow pattern considering all three forces \vec{F}_B , \vec{F}_L and \vec{F}_T at 9600 s, which is the end of the previous arc-stabilizing current period and the beginning of the next period. The \vec{F}_T induces a rotational swirl flow around a central axis, generating a centrifugal force that acts radially outward. This centrifugal force is proportional to the square of the swirl velocity and leads to the establishment of a radial pressure gradient within the melt. Near the solidification front, due to the resistance of the mushy zone, the swirl velocity is slowed down. It creates a local imbalance between the radial pressure and the centrifugal force, which prompts the melt to flow toward the bottom center of the molten pool (i.e., Ekman Pumping) [5]. As a result, the application of external AMF enhances the aforementioned counterclockwise secondary flow within the vertical section of the molten pool.

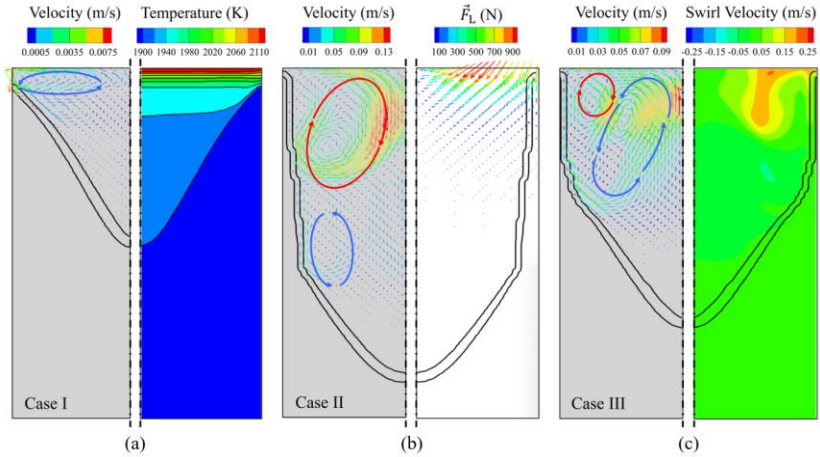


Fig. 4.4. The flow field (left) and influencing factors (right) at 9600 s. (a) Case I, velocity and temperature, (b) Case II, velocity and \vec{F}_L , (c) Case III, velocity and swirl velocity. The molten pool shape is marked with a liquid volume fraction of $f_\ell = 0.1$ and 0.9 .

Fig. 4.5 presents the evolution of \vec{F}_T and flow field during the entire arc-stabilizing current period ($t_0 = 9600$ s). The upper part of the results at each moment presents the distribution of \vec{F}_T , while the lower left side illustrates the melt flow velocity vector in the vertical section, and the lower right side displays the distribution of the swirl velocity component. When \vec{F}_T experiences a sudden change of direction, the inertia of the melt inhibits an immediate reversal of the rotational motion. From the moment of this change until t_0+2 s, the positive swirl velocity gradually decreases, ultimately approaching zero by t_0+4 s. During this interval, the counterclockwise secondary flow within the vertical section diminishes gradually. The influence of \vec{F}_T weakens, the flow driven by \vec{F}_L becomes more pronounced, resulting in a strong “periphery upward” clockwise flow within the molten pool. As the negative swirl velocity continues to increase, the rotational motion once again facilitates the establishment of the counterclockwise secondary flow in the vertical section. At t_0+8 s, when \vec{F}_T is close to its reversal, the negative swirl velocity reaches its peak, coinciding with the maximum flow rate and amplitude of the counterclockwise secondary flow. Following the subsequent reversal of \vec{F}_T , the dynamics of the counterclockwise secondary flow and positive rotational velocity mirror the earlier behaviors observed in this period. By the end of this period, at t_0+16 s, the flow pattern within the vertical section closely resembles that observed at t_0 s.

The results indicate that the introduction of \vec{F}_T significantly inhibits the influence of \vec{F}_L . However, as the direction of \vec{F}_T reverses, the inhibitory effect gradually vanishes, allowing the flow driven by \vec{F}_L to increase. Once the direction is fully reversed, the influence of \vec{F}_T begins to recover, exerting a notable inhibitory effect

on the melt flow induced by \vec{F}_L . Furthermore, it is essential to notice that the response of the swirl velocity cannot perfectly follow the directional reversal of \vec{F}_T , exhibiting a lag of approximately 4 s.

Fig. 4.6 illustrates the results of macrosegregation of the above three cases. When only \vec{F}_B is considered, the melt flow is predominantly concentrated in the upper region of the molten pool, resulting in relatively low flow velocities and a very weak macrosegregation. However, this is a theoretical and unrealistic case for VAR. When the influence of \vec{F}_L is considered, a pronounced “downward flow” develops in the central area of the ingot. This vigorous flow transports high-temperature melt from the upper portion of the molten pool to the bottom, hindering solidification and increasing the depth of the molten pool. Additionally, the enhanced flow facilitates solute transport within the molten pool, resulting in significant negative segregation on the periphery and positive segregation in the central region of the ingot. Consequently, the degree of macrosegregation is maximized under these conditions. The introduction of external alternative AMF serves to effectively mitigate the velocity and extent of the melt flow as induced by \vec{F}_L . This reduction in flow intensity leads to a considerable weakening of solute transport, resulting in a decrease of macrosegregation in both the peripheral and central areas of the ingot.

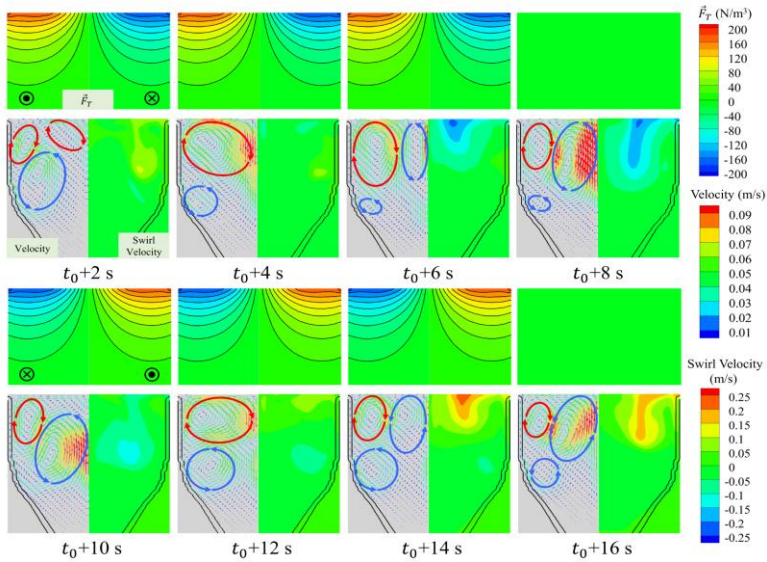


Fig. 4.5. The influence of the alternative AMF on the melt flow in the molten pool. Results during one period (from 9600 s to 9616 s) with every 2 s of interval are shown: \vec{F}_T and its direction, velocity vectors in the vertical section, and the magnitude of the swirl velocity component.

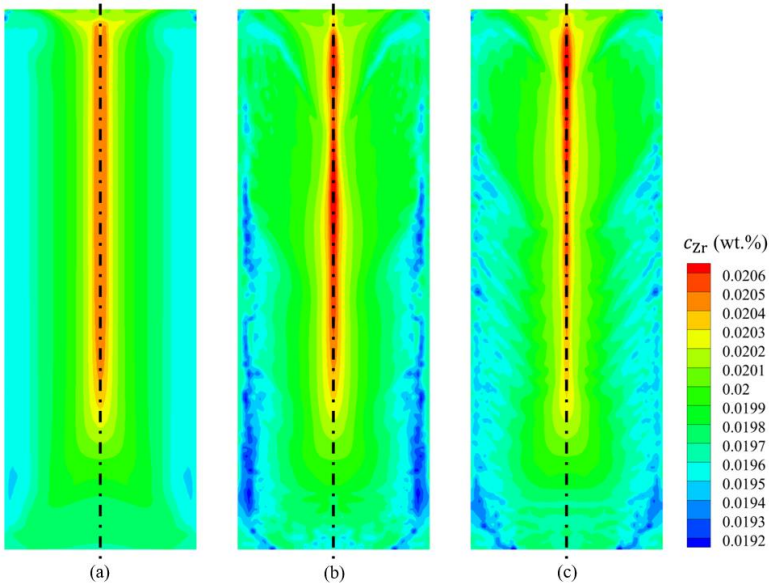


Fig. 4.6. The distribution of solute element Zr in the final ingot. (a) Case I, considering only \vec{F}_B , (b) Case II, considering \vec{F}_B and \vec{F}_L , and (c) Case III, considering \vec{F}_B , \vec{F}_L and \vec{F}_T .

4.5 CONCLUSIONS

2D axisymmetric simulations of the solidification process during VAR with the commercial software ANSYS Fluent were performed. The simulated molten pool profile and segregation distribution are qualitatively consistent with the experimental results. As the main goal of this study is to investigate the effect of the applied alternative AMF on the macrosegregation result, a numerical parameter study was performed by performing simulations of three cases: Case I, considering only combined thermal and solute-driven buoyancy \vec{F}_B , Case II, considering both \vec{F}_B and the self-induced electromagnetic force \vec{F}_L , Case III, considering all \vec{F}_B , \vec{F}_L and the AMF-induced electromagnetic force \vec{F}_T .

The applied AMF generates an electromagnetic force \vec{F}_T in the tangential direction, creating a rotational swirl flow and a centrifugal force directed radially outward. Consequently, a secondary flow along the side walls towards the bottom center within the molten pool is induced. This modified flow pattern in the molten pool helps reduce macrosegregation in VAR ingots, hence improving the service life and mechanical properties of aviation titanium alloys.

A qualitative agreement between the simulation and experiment regarding the molten pool contour and segregation profile was achieved. Nevertheless, some key phenomena regarding the formation of as-cast structures were not considered

by the current model. As a further step, a model extension by considering the multiphase flow and mixed columnar-equiaxed solidification is suggested [16].

CONFERENCE DISCLAIMER

Abstract part of this manuscript was previously presented at the conference: The 8th International Conference on Solidification and Gravity dated from 02 th September to 05th September 2024 in Miskolc - Lillafüred, Hungary, Web Link of the proceeding: <https://www.solgrav.uni-miskolc.hu/SG24-Program&Abstracts.pdf>

DISCLAIMER (ARTIFICIAL INTELLIGENCE)

Author(s) hereby declare that NO generative AI technologies such as Large Language Models (ChatGPT, COPILOT, etc.) and text-to-image generators have been used during the writing or editing of this manuscript.

COMPETING INTERESTS

Authors have declared that no competing interests exist.

REFERENCES

1. Xu J, Zeng W, Jia Z, Sun X, Zhou J, Static globularization kinetics for Ti-17 alloy with initial lamellar microstructure, *J. Alloys Compd.* 2014;603:239–247.
Available:<https://doi.org/10.1016/j.jallcom.2014.03.082>
2. Shi X, Zeng W, Zhao Q, The effects of lamellar features on the fracture toughness of Ti-17 titanium alloy, *Mater. Sci. Eng. A.* 2015;636:543–550.
Available:<https://doi.org/10.1016/j.msea.2015.04.021>
3. Kondrashov EN, Rusakov KA, Shchetnikov NV, Leder MO, Segregation Defects in VAR Titanium Alloys: I. Common Defects, *Russ. Metall. Met.* 2022;2022:553–558.
Available:<https://doi.org/10.1134/S0036029522060118>.
4. Davidson PA, Kinnear D, Lingwood RJ, Short DJ, He X, The role of Ekman pumping and the dominance of swirl in confined flows driven by Lorentz forces, *Eur. J. Mech. – Bfluids.* 1999;18:693–711.
Available:[https://doi.org/10.1016/s0997-7546\(99\)00106-5](https://doi.org/10.1016/s0997-7546(99)00106-5)
5. Davidson PA, He X, Lowe AJ, Flow transitions in vacuum arc remelting, *Mater. Sci. Technol.* 2000;16:699–711.
Available:<https://doi.org/10.1179/026708300101508306>
6. Kondrashov EN, Musatov MI, Maksimov AYu, Goncharov AE, Konovalov LV, Calculation of the molten pool depth in vacuum arc remelting of alloy Vt3-1, *J. Eng. Thermophys.* 2007;16:19–25.
Available:<https://doi.org/10.1134/S1810232807010031>
7. Karimi-Sibaki E, Kharicha A, Abdi M, Vakhrushev A, Wu M, Ludwig A, Bohacek J, A numerical study on the influence of an axial magnetic field (AMF) on Vacuum Arc Remelting (VAR) Process, *Metall. Mater. Trans. B* 2021;52:3354–3362.

- Available:<https://doi.org/10.1007/s11663-021-02264-w>
8. Karimi-Sibaki E, Kharicha A, Vakhrushev A, Abdi M, Wu M, Ludwig A, Bohacek J, Preiss B, Numerical modeling and experimental validation of the effect of arc distribution on the as-solidified Ti64 ingot in vacuum arc remelting (VAR) process, *J. Mater. Res. Technol.* 2022;19:183–193.
Available:<https://doi.org/10.1016/j.jmrt.2022.05.036>
 9. Xiong Y, Liu Z, Zhao Z, Li B, Numerical investigation on the evolution behavior of solidification structure in titanium alloy during vacuum arc remelting process, *Metall. Mater. Trans.* 2024;B 55:4182–4199.
Available:<https://doi.org/10.1007/s11663-024-03316-7>
 10. Wang X, Liu Z, Wang F, Zhao Z, Baleta J, Li B, Effect of current intensity on molten pool and solidification in vacuum arc remelting process of Ti60 alloy, *Ironmak. Steelmak. Process. Prod. Appl.* 2024;51:931–946.
Available:<https://doi.org/10.1177/03019233241259280>
 11. Deng G, Xia Z, Ma C, Guo Y, Sun Z, Zhang M, Chen Q, Li Q, Shen Z, Ding B, Zheng T, Liu C, Zhong Y. Effect of alternative magnetic fields with different intensities on microstructure and mechanical properties of M50 steel during vacuum arc remelting, *J. Iron Steel Res. Int;* 2024.
Available:<https://doi.org/10.1007/s42243-024-01355-7>
 12. Voller VR, Swaminathan CR, Eral source-based method for solidification phase change, *Numer. Heat Transf. Part B Fundam.* 1991;19:175–189.
Available:<https://doi.org/10.1080/10407799108944962>
 13. Voller VR, Brent AD, Prakash C, The modelling of heat, mass and solute transport in solidification systems, *Int. J. Heat Mass Transf.* 1989;32:1719–1731.
Available:[https://doi.org/10.1016/0017-9310\(89\)90054-9](https://doi.org/10.1016/0017-9310(89)90054-9)
 14. Reiter G, Maronnier V, Sommitsch C, Gäumann M, Schützenhöfer W, Numerical simulation of the VAR process with CALCOSOFT-2D and its validation, in. 2003;77–86.
 15. Bellet M, Combeau H, Fautrelle Y, Gobin D, Rady M, Arquis E, Budenkova, B. Dussoubs, Y. Duterrail, A. Kumar, C.A. Gandin, B. Goyeau O, Mosbah S, Založnik M, Call for contributions to a numerical benchmark problem for 2D columnar solidification of binary alloys, *Int. J. Therm. Sci.* 2009;48:2013–2016.
Available:<https://doi.org/10.1016/j.ijthermalsci.2009.07.024>
 16. Wu M, Ludwig A, Kharicha A, Volume-averaged modeling of multiphase flow phenomena during alloy solidification, *Metals.* 2019;9:229.
Available:<https://doi.org/10.3390/met9020229>.

Disclaimer/Publisher's Note: The statements, opinions and data contained in all publications are solely those of the individual author(s) and contributor(s) and not of the publisher and/or the editor(s). This publisher and/or the editor(s) disclaim responsibility for any injury to people or property resulting from any ideas, methods, instructions or products referred to in the content.

© Copyright (2025): Author(s). The licensee is the publisher (BP International).

Peer-Review History:

This chapter was reviewed by following the Advanced Open Peer Review policy. This chapter was thoroughly checked to prevent plagiarism. As per editorial policy, a minimum of two peer-reviewers reviewed the manuscript. After review and revision of the manuscript, the Book Editor approved the manuscript for final publication. Peer review comments, comments of the editor(s), etc. are available here: <https://peerreviewarchive.com/review-history/3590.4>